



MOX-Report No. 01/2017

Rayleigh-Taylor instability in soft elastic layers

Riccobelli, D.; Ciarletta, P.

MOX, Dipartimento di Matematica
Politecnico di Milano, Via Bonardi 9 - 20133 Milano (Italy)

mox-dmat@polimi.it

<http://mox.polimi.it>

Rayleigh–Taylor instability in soft elastic layers

D. Riccobelli¹ and P. Ciarletta¹,

¹ MOX–Dipartimento di Matematica, Politecnico di Milano,
piazza Leonardo da Vinci 32, 20133 Milano, Italy.

January 4, 2017

Abstract

This work investigates the morphological stability of a soft body composed of two heavy elastic layers, attached to a rigid surface and subjected only to the bulk gravity force. Using theoretical and computational tools, we characterize the selection of different patterns as well as their nonlinear evolution, unveiling the interplay between elastic and geometric effects for their formation.

Unlike similar gravity-induced shape transitions in fluids, as the Rayleigh–Taylor instability, we prove that the nonlinear elastic effects saturate the dynamic instability of the bifurcated solutions, displaying a rich morphological diagram where both digitations and stable wrinkling can emerge. The results of this work provide important guidelines for the design of novel soft systems with tunable shapes, with several applications in engineering sciences.

1 Introduction

Shape transitions in soft solids result from a bifurcation of the elastic solutions driven by either geometrical or constitutive nonlinearities. The characterization of the emerging morphologies is the object of morpho-elasticity, a recent branch of continuum mechanics at the interface between finite elasticity and perturbation theory. This vibrant research field has rapidly developed in the last decade, pushed by the technological availability of experimental devices controlling the extreme deformations of soft incompressible materials, such as hydrogels [1, 2, 3] and elastomers [4, 5].

Although their boundary value problems are intrinsically different, the study of pattern formation in soft solids has highlighted some similarities, yet several relevant differences, with the instability characteristics of hydrodynamic systems. For example, if the surface tension in a thin fluid filament triggers the formation of droplets, which spontaneously break down [6], such a dynamics can be stabilised by elastic effects in soft solid cylinders [7], thus driving the emergence of stable beads-on-a-string patterns [8]. Similarly, whilst fingering at the interface of two immiscible viscous fluids is an unstable process [9], stable digitations may occur after a subcritical bifurcation for a fluid pushing against an elastic surface [10] and at the interface between a thin elastic layer adhering to a glass plate [11].

Another interesting example is the gravity-induced instability in an elastic layer attached to a rigid substrate with a traction-free surface facing downwards. Contrarily to gravity waves in a fluid layer, the free surface experiences fluctuations that eventually saturate when the large deformations store an elastic free energy of the same order as the corresponding variation of the potential energy. The linear stability analysis of this problem has been recently performed [12], then refined to consider the effect of an applied strain on the elastic layer [13]. Nonetheless, this problem had been previously solved using numerical techniques [14], often being used as a test case to study the stability of discrete solutions, obtained by means of mixed finite element techniques [15, 16].

Since Rayleigh [17] and Taylor [18], it is well known that the horizontal interface between one fluid layer put on top of a lighter one is unstable to perturbation of long wavelength, i.e. bigger than the capillary length, forming protrusions growing with a characteristic time. However, if one takes surface tension into account, the growth of small wavelength protrusions is inhibited by capillary effects, thus larger wavelength drops grow and eventually drip [19]. In this work, we aim at studying this kind of gravity instability in a soft system made of two heavy elastic layers attached on one end to a rigid surface. In particular, we are interested in characterizing both pattern formation and its nonlinear evolution, determining the interplay between elastic and geometric effects for the emergence of a given pattern.

The article is organized as follows. In Section 2, we define the nonlinear elastic problem and identify its basic solution. In Section 3, we perform the linear stability analysis of the problem, deriving the marginal stability curves as a function of the elastic and geometric dimensionless parameters. In Section 4, we perform numerical simulations using finite elements for studying pattern formation in the fully nonlinear regime. In Section 5, we finally discuss the theoretical and numerical results, adding a few concluding remarks.

2 The non-linear elastic problem and its basic solution

In a Cartesian coordinate system with unit base vectors \mathbf{E}_i , with $i = (X, Y, Z)$, we consider a soft body made of two hyperelastic layers, as sketched in Figure 1.

Let \mathbb{E}^3 be the three-dimensional Euclidean space, the body occupies a domain $\Omega \subset \mathbb{E}^3$, having a thickness H along the Y axis and a length L along the X axis, with $L \gg H$. We also consider that the body is infinitely long along the Z direction, so that a plane strain assumption can be made, hence

$$\Omega = (0, L) \times (0, H) \times \mathbb{R}.$$

The body is clamped to a rigid substrate at $Y = 0$, so that its volume Ω can be split in the two subdomains Ω_a and Ω_b occupied by the constituting layers, such that:

$$\begin{aligned} \Omega_a &= \{\mathbf{X} \in \Omega \mid 0 < Y < H_a\}, \\ \Omega_b &= \{\mathbf{X} \in \Omega \mid H_a < Y < H\}, \end{aligned}$$

where \mathbf{X} is the material position vector, H_a and H_b are the thicknesses of the layers.

Indicating $\mathbf{x} = \mathbf{x}(X, Y)$ the spatial position vector, the kinematics is described by the geometrical deformation tensor $\mathbf{F} = \text{Grad } \mathbf{x}$. We also assume that the layers behave as incompressible neo-Hookean materials and the strain energy density of each layer is given by

$$W_\beta(\mathbf{F}) = \frac{\mu_\beta}{2} (I_1 - 2) - p(\det \mathbf{F} - 1), \quad \beta = (a, b); \quad (1)$$

where I_1 is the trace of the right Cauchy–Green tensor $\mathbf{C} = \mathbf{F}^T \mathbf{F}$ and p is the Lagrangian multiplier enforcing the internal constraint of incompressibility.

Using the constitutive assumption in Eq. (1), the first Piola-Kirchhoff stress tensor \mathbf{S} reads:

$$\mathbf{S}_\beta = \frac{\partial W_\beta}{\partial \mathbf{F}} = \mu_\beta \mathbf{F}^T - p \mathbf{F}^{-1}, \quad \beta = (a, b).$$

Assuming quasi-static conditions, the balance of linear momentum for the elastic body subjected to its own weight reads:

$$\text{Div } \mathbf{S}_\beta + \rho_\beta \mathbf{g} = 0 \quad \text{in } \Omega_\beta, \quad \text{where } \beta = (a, b); \quad (2)$$

where Div is the material divergence, ρ_a and ρ_b are the densities of the layers, $\mathbf{g} = g \mathbf{E}_Y$, is the gravity acceleration vector.

In the following we aim to provide a unified analysis of the two configurations depicted in Figure 1. For the sake of notational compactness, we consider that a positive g represents the body hanging down a rigid wall (Figure 1(a)), and a negative g the body placed on top of a rigid substrate (Figure 1(b)).

The two boundary conditions at the fixed substrate and at the free surface read

$$\begin{cases} \mathbf{S}_b^T \mathbf{E}_Y = \mathbf{0} & \text{for } Y = H, \\ \mathbf{E}_Y \cdot \mathbf{S}_\beta^T \mathbf{E}_X = 0 & \text{for } X = (0, L), \beta = (a, b) \\ \mathbf{u} = \mathbf{0} & \text{for } Y = 0, \\ \mathbf{u} \cdot \mathbf{E}_X = 0 & \text{for } X = (0, L); \end{cases} \quad (3)$$

where $\mathbf{u} = (\mathbf{x} - \mathbf{X})$ is the displacement vector field. The elastic boundary value problem is finally complemented by the following displacement and stress

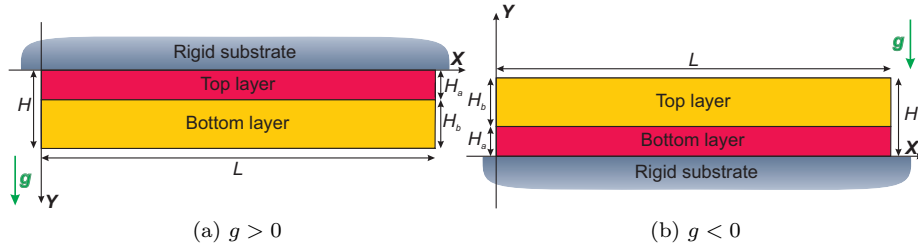


Figure 1: Sketch of the material setting in two different configurations. Case (a): the body hangs below on a fixed rigid wall, thus being subjected to a tensile gravity force along Y (left). Case (b): the body is placed on top of a rigid substrate, thus being subjected to a compressive gravity force along Y (right).

continuity conditions at the interface between the two layers, respectively

$$\begin{cases} \lim_{Y \rightarrow H_a^-} \mathbf{u} = \lim_{Y \rightarrow H_a^+} \mathbf{u}, \\ \lim_{Y \rightarrow H_a^-} \mathbf{S}_a^T \mathbf{E}_Y = \lim_{Y \rightarrow H_a^+} \mathbf{S}_b^T \mathbf{E}_Y. \end{cases} \quad (4)$$

The boundary value problem Eqs. (2)–(4) admits a basic solution given by

$$\mathbf{u} = \mathbf{0}, \quad p = \begin{cases} \mu_a + \rho_a g(Y - H_a) - \rho_b g H_b & \text{for } 0 < Y < H_a, \\ \mu_b + \rho_b g(Y - H) & \text{for } H_a < Y < H; \end{cases} \quad (5)$$

so that no basic deformation is allowed by the incompressibility constraint, and the body is subjected to a hydrostatic pressure linearly dependent on Y . We also highlight that the pressure field in Eq. (5) is discontinuous if $\mu_a \neq \mu_b$ or $\rho_a \neq \rho_b$.

3 Linear stability analysis of the basic solution

3.1 Incremental equations

We now aim at investigating the stability of the basic elastic solution Eq. (5) using the method of incremental deformations superposed on a finite strain [20].

Let us perturb the basic configuration by applying an incremental displacement $\delta \mathbf{u}$, if we set $\delta \mathbf{F} = \text{Grad } \delta \mathbf{u}$, the linearised incremental Piola-Kirchhoff stress tensor is

$$\delta \mathbf{S}_\beta = \mathcal{A}_0^\beta : \delta \mathbf{F} + p \delta \mathbf{F} - \delta p \mathbf{I} \quad \text{for } \beta = (a, b);$$

where

$$\mathcal{A}_0^\beta = \frac{\partial^2 W_\beta}{\partial \mathbf{F} \partial \mathbf{F}}; \quad \text{with} \quad \mathcal{A}_{0ijhk}^\beta = \frac{\partial^2 W_\beta}{\partial F_{ji} \partial F_{kh}}$$

is the tensor of instantaneous elastic moduli, \mathbf{I} is the identity tensor, δp is the increment of the Lagrangian multiplier p and the two dots operator $(:)$ denotes the double contraction of the indices, namely

$$(\mathcal{A}_0^\beta : \delta \mathbf{F})_{ij} = \mathcal{A}_{0ijhk}^\beta \delta F_{kh}.$$

Recalling that the basic solution is undeformed, the incremental incompressibility and equilibrium equations read, respectively

$$\text{Div } \delta \mathbf{S}_\beta = \mathbf{0} \quad \text{in } \Omega_\beta, \quad \text{with } \beta = (a, b), \quad (6)$$

$$\text{Div } \delta \mathbf{u} = 0 \quad \text{in } \Omega. \quad (7)$$

The incremental counterparts of two boundary conditions at the fixed substrate and at the free surface may be rewritten as, respectively

$$\begin{cases} \delta \mathbf{S}_b^T \mathbf{E}_Y = \mathbf{0} & \text{for } Y = H, & (8) \\ \mathbf{E}_Y \cdot \delta \mathbf{S}_\beta^T \mathbf{E}_X = \mathbf{0} & \text{for } X = (0, L), \beta = (a, b), & (9) \\ \delta \mathbf{u} = \mathbf{0} & \text{for } Y = 0, & (10) \\ \delta \mathbf{u} \cdot \mathbf{E}_X = 0 & \text{for } X = (0, L). & (11) \end{cases}$$

Similarly, the incremental versions of the displacement and stress continuity conditions at the interface read:

$$\begin{cases} \lim_{Y \rightarrow H_a^-} \delta \mathbf{u} = \lim_{Y \rightarrow H_a^+} \delta \mathbf{u}, \\ \lim_{Y \rightarrow H_a^-} \delta \mathbf{S}_a^T \mathbf{E}_Y = \lim_{Y \rightarrow H_a^+} \delta \mathbf{S}_b^T \mathbf{E}_Y. \end{cases} \quad (12)$$

$$\begin{cases} \lim_{Y \rightarrow H_a^-} \delta \mathbf{S}_a^T \mathbf{E}_Y = \lim_{Y \rightarrow H_a^+} \delta \mathbf{S}_b^T \mathbf{E}_Y. \end{cases} \quad (13)$$

In the following, we derive the solution of the incremental boundary value problem given by Eqs. (6)-(13).

3.2 Solution of the incremental boundary value problem

Let us now assume an ansatz by variable separation in the expression of the incremental displacement, namely

$$\delta \mathbf{u} = U(Y) \sin(kX) \mathbf{E}_X + V(Y) \cos(kX) \mathbf{E}_Y, \quad (14)$$

where k is the horizontal spatial wavenumber. We recall that such a functional dependence along the X direction suitably describes both the infinite geometry, for which k is a continuous variable, and a finite length L , so that $k = 2\pi n/L$ with integer mode n .

From Eq. (7) we get that

$$kU(Y) = -V'(Y). \quad (15)$$

From the first component of Eq. (6) we obtain the expression for δp as

$$\delta p = \cos(kX) (\rho_\beta g V(Y) - \mu_\beta V'(Y) + k^{-2} \mu_\beta V'''(Y)) \quad \text{in } \Omega_\beta \text{ with } \beta = (a, b). \quad (16)$$

By substituting Eqs. (15) and (16) in the second component of Eq. (6), we obtain the following ordinary differential equation:

$$V''''(Y) - 2k^2 V''(Y) + k^4 V(Y) = 0, \quad (17)$$

which is valid for both layers and whose solution is given by:

$$V(Y) = C_{1\beta} e^{-kY} + C_{2\beta} Y e^{-kY} + C_{3\beta} e^{kY} + C_{4\beta} Y e^{kY} \quad \text{in } \Omega_\beta, \beta = (a, b). \quad (18)$$

Hence, setting

$$\mathbf{v} = \left[\frac{C_{1a}}{H_a}, C_{2a}, \frac{C_{3a}}{H_a}, C_{4a}, \frac{C_{1b}}{H_a}, C_{2b}, e^{2kH_a} \frac{C_{3b}}{H_a}, e^{2kH_a} C_{4b} \right]^T$$

we impose the conditions given in Eqs. (8)–(13), we find 8 linear algebraic equations in the unknowns v_j , $j = (1, \dots, 8)$, so that we can write such system in the compact form $\mathbf{M}\mathbf{v} = \mathbf{0}$ where \mathbf{M} is the 8×8 coefficients' matrix. Hence, we find that a non-null solution of such linear system exists if and only if

$$\det \mathbf{M} = 0; \quad (19)$$

The full form of \mathbf{M} is reported in the Appendix A.

3.3 Results of the linear stability analysis

Let us now discuss the results of the linear stability analysis by making use of the following dimensionless parameters:

$$\gamma = \frac{\rho_a g H_a}{\mu_a}, \quad \alpha_H = \frac{H_b}{H_a}, \quad \alpha_\mu = \frac{\mu_b}{\mu_a}, \quad \alpha_\rho = \frac{\rho_b}{\rho_a}, \quad \tilde{k} = H_a k.$$

A great simplification arises if we set both $\alpha_\rho = 1$ and $\alpha_\mu = 1$ or if we impose $\alpha_H = 0$ in Eq. (19), so that the body is made of a single homogeneous slab. In particular, we recover the same expression reported in [12]:

$$\frac{\rho g H}{\mu_a} = \frac{2kH \left(2(kH)^2 + \cosh(2kH) + 1 \right)}{\sinh(2kH) - 2kH};$$

highlighting that an elastic bifurcation occurs for the critical value $\frac{\rho g H}{\mu_a} \simeq 6.22$ with critical wavenumber $kH \simeq 2.11$.

Let us now analyse the resulting solutions when $\alpha_\rho = 1$, namely assuming that the body force is the same for both layers. In the case in which $\alpha_\mu \neq 1$ or $\alpha_H \neq 1$, we find only one root of equation Eq. (19). In Figure 2 we depict the resulting marginal stability curves varying the parameters α_μ and α_H .

We denote by γ_{cr} the critical value of γ , i.e. the minimum value of the marginal stability curve obtained fixing α_H and α_μ . We denote by \tilde{k}_{cr} the critical wavenumber, namely the value of \tilde{k} for which the marginal stability curve has a minimum. All the critical values of the marginal stability curves have been found by using the Newton's method with the software *Mathematica* 11.0 (Wolfram Research, Champaign, IL, USA).

In Figure 3 we plot the critical values γ_{cr} and \tilde{k}_{cr} when varying α_H and α_μ . We find that γ_{cr} strongly depends on α_μ and α_H . In Figure 3(a) we find that if we increase the parameter α_μ the critical value γ_{cr} also increases, so that high values of α_μ have a stabilizing effect. On the contrary, in Figure 3(c) we find that if we increase α_H the critical value γ_{cr} decreases. We highlight that, if α_H tends to zero we obtain that $\gamma_{cr} \simeq 6.22$, which is the single layer

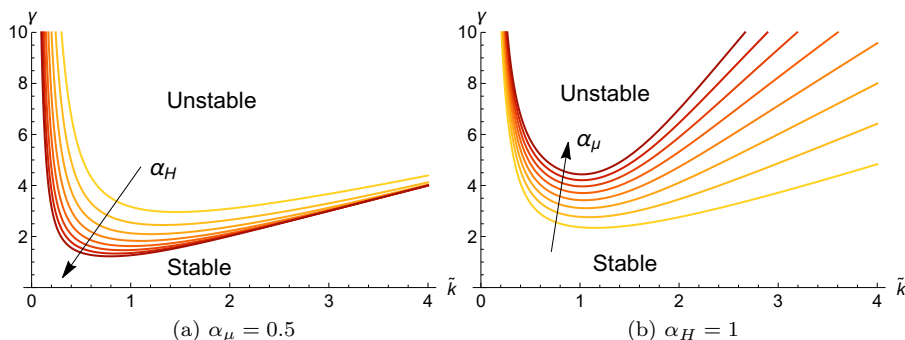


Figure 2: Marginal stability curves showing the order parameter γ versus the horizontal wavenumber \tilde{k} for $\rho_a = \rho_b$ and: (a) $\alpha_\mu = 0.5$, (b) $\alpha_H = 1$. The curves are shown at varying α_H (a) and α_μ (b) from 0.6 to 2 by steps of 0.2, the arrow indicates the direction in which the parameter grows.

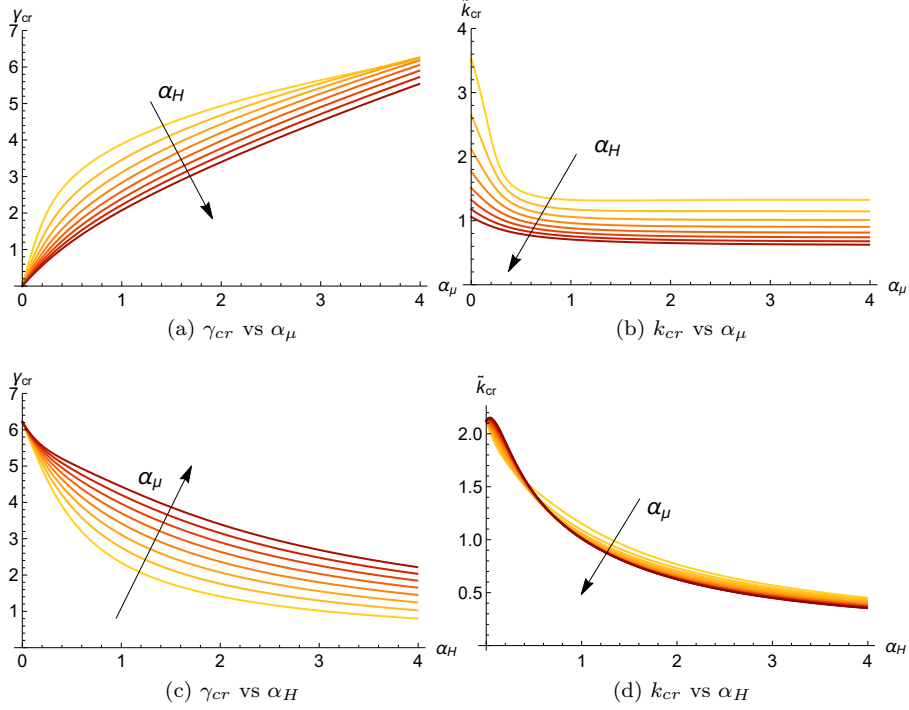


Figure 3: Plot of the critical values of (a) γ_{cr} versus α_μ at varying α_H ; (b) γ_{cr} versus α_H at varying α_μ ; (c) \tilde{k}_{cr} versus α_μ at varying α_H ; (d) \tilde{k}_{cr} versus α_H at varying α_μ . The arrows indicate the direction in which the parameters α_H (a,b) and α_μ (c,d) grow from 0.6 to 2 by steps of 0.2.

limit discussed before. The same limit is found for α_μ tending to zero, since it represents the case in which the bottom layer in Figure 1(a) becomes infinitely soft. The critical wavelength is always of the same order of the body thickness, resulting to be more influenced by the parameter α_H if $\alpha_\mu > 1$, as we can notice from Figures 3(b) and 3(d).

The case in which $\alpha_\rho = 1$ is of particular interest in the applications because it is reproducible in experiments using hydrogels. In fact, these soft materials are mainly composed of water, thus having a density which is of the order of 10^3 kg/m^3 . Nonetheless, by small variation of the crosslink concentration, it is possible to obtain a shear modulus μ ranging from 100 Pa to 10 kPa. For example, if we consider two hydrogel layers with $H_a = H_b$ (Figure 2(b)), where the clamped one has $\mu_a = 300 \text{ Pa}$ and the other $\mu_b = 600 \text{ Pa}$, we find that $\gamma_{cr} \simeq 4.4366$. Accordingly, an instability would appear at $H_a \geq \mu_a \gamma_{cr} / (\rho g) \simeq 13.57 \text{ cm}$.

The general case in which $\alpha_\rho \neq 1$ is a bit more complex, in fact Eq. (19) can be written in the following compact form

$$c_1 \gamma^2 + c_2 \gamma + c_3 = 0 \quad (20)$$

where the coefficients c_1 , c_2 and c_3 depend on α_H , α_μ , α_ρ and \tilde{k} , as reported in the Appendix B.

Even if their expressions are very cumbersome, we can still make some general observations. In fact we observe that c_1 does not depend on α_ρ whereas, if we fix the other variables, c_3 has a different sign if $\alpha_\rho > 1$ or if $0 < \alpha_\rho < 1$. Hence, one of the two real roots of Eq. (20) changes sign if we consider $\alpha_\rho > 1$ or $0 < \alpha_\rho < 1$.

Thus, we make a distinction in the following between these two cases, which physically correspond to the two configurations depicted in Figure 1.

3.3.1 Case (a): free surface instability ($\gamma > 0$)

The configuration shown in Figure 1(a) undergoes a morphological transition if Eq. (20) possesses at least a positive root for γ , since we assume $g > 0$.

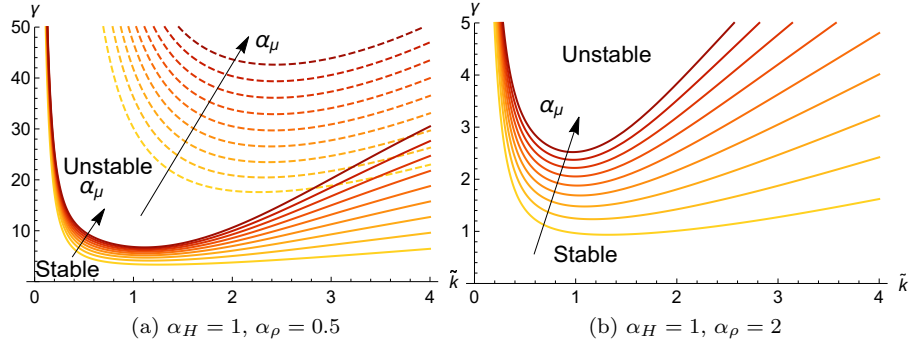


Figure 4: Marginal stability curves showing the order parameter γ versus the horizontal wavenumber \tilde{k} for $\alpha_H = 1$ and: (a) $\alpha_\rho = 0.5$, (b) $\alpha_\rho = 2$ where α_μ varies from 0.4 to 2 by steps of 0.2. In (a) we find two positive solutions (solid and dashed lines) of equation Eq. (20) whereas in Figure (b) we only find one positive solution.

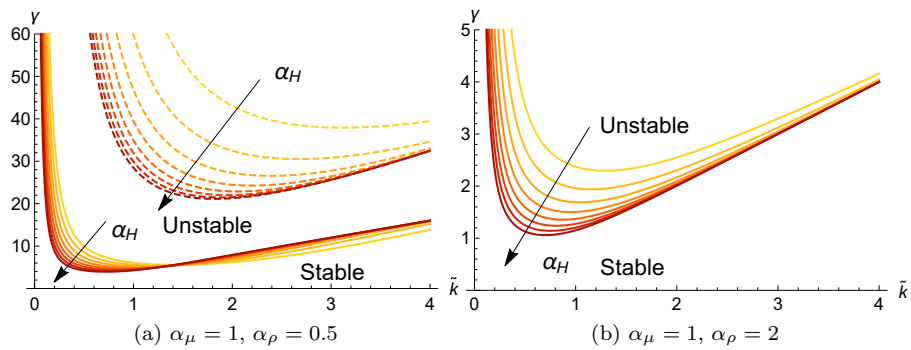


Figure 5: Marginal stability curves showing the order parameter γ versus the horizontal wavenumber \tilde{k} for $\alpha_\mu = 1$ and: (a) $\alpha_\rho = 0.5$, (b) $\alpha_\rho = 2$ with α_H varying from 0.6 to 2 by steps of 0.2. In (a) we find two positive solutions (solid and dashed lines) of equation Eq. (20) whereas in Figure (b) we only find one positive solution.

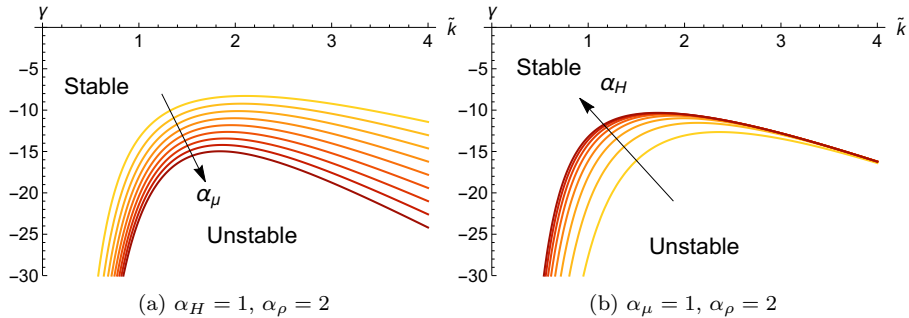


Figure 6: Marginal stability curves showing the negative root of the order parameter γ versus the horizontal wavenumber \tilde{k} for $\alpha_\rho = 2$ and: (a) $\alpha_H = 1$ with α_μ varying from 0.4 to 2 by steps of 0.2; (b) $\alpha_\mu = 1$ with α_H varying from 0.6 to 2 by steps of 0.2.

In Figures 4 and 5 we depict the marginal stability curves $\gamma(\tilde{k})$ when we vary the parameters α_H , α_ρ and α_μ in Eq. (20). In this case, we find that the instability is localised at the free boundary of the slab, i.e. at $Y = H$.

We can observe that we have the same behaviour discussed for the case $\alpha_\rho = 1$: if we increase the parameter α_μ we obtain a stabilization of the system (i.e. γ_{cr} increases) whereas if we decrease α_H we have instability for lower values of γ .

3.3.2 Case (b): interfacial instability ($\gamma < 0$)

Conversely, the configuration shown in Figure 1(b) undergoes a morphological transition if Eq. (20) possesses a negative root for γ , since we assume $g < 0$. As previously discussed, this happens only if $\alpha_\rho > 1$, meaning that the top layer is heavier than the bottom one. Thus, this case is the elastic analog of the Rayleigh-Taylor instability. As found in fluids, the instability is concentrated at the interface between the layers and decays away from it.

In this configuration, we define the critical value γ_{cr} as the maximum of the marginal stability curve $\gamma(\tilde{k})$ for fixed α_H , α_μ , and α_ρ .

In Figure 6 we set $\alpha_\rho = 2$ and we plot the marginal stability curves for several values of the parameters α_H and α_μ . Also in this case we highlight that increasing the parameter α_μ stabilizes the system, whereas an increase of the parameter α_H favours the onset of the interfacial instability.

In the next section, based on the results of the linear stability analysis, we build the simulation tools for studying the fully nonlinear morphological transition.

4 Post-buckling analysis

In this section we numerically implement the fully non-linear problem given by Eqs. (2)-(4). We finally report the results of numerical simulations for the two cases under considerations, highlighting the morphological evolution of the emerging patterns in the fully nonlinear regime.

4.1 Finite element implementation

The boundary value problem is implemented by using the open source tool for solving partial differential equations FEniCS [21]. In order to enforce the incompressibility constraint, a mixed formulation has been chosen. If the two layers have different stiffness or mass density, the pressure field may present a discontinuity at the interface between the two layers, according to the basic solution Eq. (5). Accordingly, we used the element P_2 - P_0 [22] in numerical simulations.

This element discretizes the displacement with piecewise quadratic functions and the pressure field with piecewise constant functions, so that we can correctly account for a discontinuous pressure field. It is also numerically stable in linear elasticity [22] and it has been successfully used in several non-linear applications [15, 14].

We use a rectangular mesh whose height is $H = 1$ and whose length is the critical wavelength $\lambda = 2\pi H_a / \tilde{k}_{cr}$, where \tilde{k}_{cr} is the critical value arising from the previous linear stability analysis and depending on α_ρ , α_H and α_μ . We set $\mathbf{u} = \mathbf{0}$ at $Y = 0$ and we impose periodic boundary conditions at $X = 0$ and $X = \lambda$. The number of elements used depends on the length of the mesh, the maximum number of elements used is 30000.

In order to investigate the post-buckling regime, we impose a sinusoidal imperfection at the top boundary of the mesh with a wavenumber k_{cr} and an amplitude $h = 10^{-4}H$ as done in [23, 24].

The solution is found by using an incremental iterative Newton–Raphson method increasing (or decreasing in the fluid analogue case) the control parameter γ . In each iteration, the calculation is performed by using the linear algebra back-end PETSc (Portable, Extensible Toolkit for Scientific Computation) and the linear system is solved through a LU (Lower-Upper) decomposition. The code automatically adjust the increment of the control parameter if γ is near the critical value γ_{cr} or when the Newton–Raphson method fails to converge.

Since secondary bifurcations may appear in such a dispersive problem, due to subharmonic resonance phenomena in the fully nonlinear regime, we performed further simulations using the approach proposed in [25]. Accordingly, we looked for period-doubling and period-tripling secondary bifurcations by using as computational domain the sets $[0, 2m\pi/k_{cr}] \times [0, 1]$ with $m = 2$ and $m = 3$, respectively. However, we did not find any further bifurcation in the parameters’ range considered in the manuscript, in agreement with the experimental observations performed in the single layer case [12].

4.2 Numerical results

In the following, we report the results of the numerical simulation for the two cases under considerations.

4.2.1 Case (a): free surface instability ($\gamma > 0$)

We first implement the case described in Figure 1(a), setting $\alpha_\rho = 1$ in order to mimic the behaviour of a slab made of two hydrogel layers. In Figure 7, we depict the results of the numerical simulations for two different values of α_μ . In particular, we highlight that the deformation is localised at the free boundary

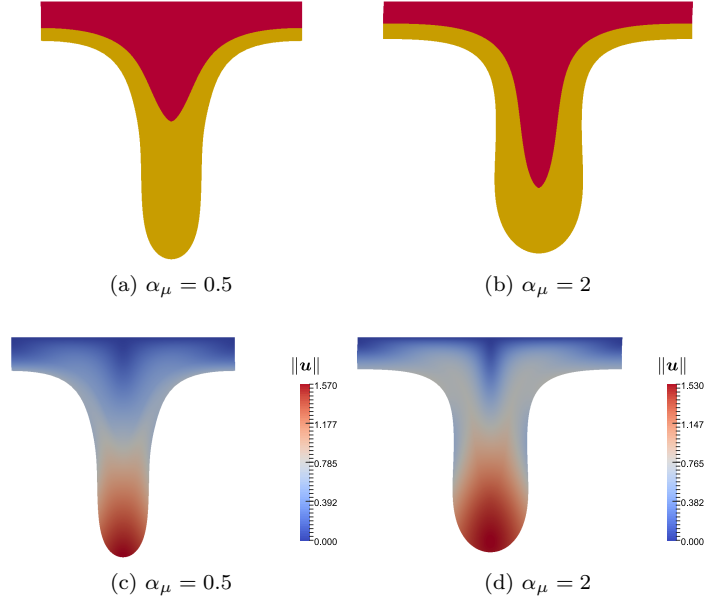


Figure 7: Resulting fingering morphology and displacement fields setting $\alpha_H = 1$, $\alpha_\rho = 1$ and (a, c) $\alpha_\mu = 0.5$ and $\gamma = 3.14$; (b, d) $\alpha_\mu = 2$ and $\gamma = 5.5$. In (c, d) the colorbars indicate the norm of the displacement.

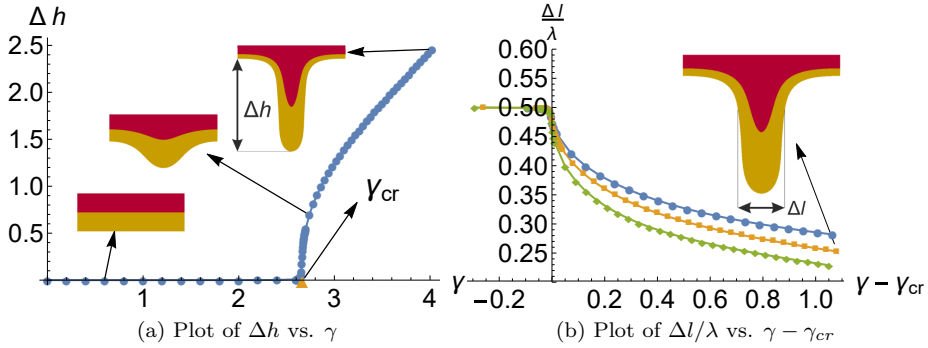


Figure 8: (a) Numerical results showing the height of the fingers Δh versus the order parameter γ , setting $\alpha_\rho = 1$, $\alpha_H = 1$, $\alpha_\mu = 0.75$. The simulations validate the marginal stability threshold $\gamma_{cr} \simeq 2.66$ predicted by the linear stability analysis. (b) Plot of the normalized fingers' thickness $\Delta l/\lambda$ for $\alpha_\mu = 0.5$ (green), 0.75 (orange) and 2 (blue).

of the body, and it evolves towards the formation of stable hanging digitations. Let Δh be the maximum vertical distance of the points on the free surface whilst Δl be the horizontal distance between the points which have initial coordinates $(\lambda/4, H)$ and $(3/4\lambda, H)$, so that $\Delta l/\lambda = 0.5$ if $\gamma < \gamma_{cr}$. Thus, we employ Δh and Δl to study the nonlinear evolution of the fingers' morphology.

As shown in Figure 8(a), we find that the fingering height Δh continuously

increases as the control parameter γ goes beyond its critical value. When performing a cyclic variation of the order parameter, where we first incremented γ until a value $\gamma_{\max} > \gamma_{cr}$ and later decreased it back to the initial value, we found that both Δh and Δl did not encounter any discontinuity, always following the same curve in both directions. Moreover, in the weakly nonlinear regime Δh increases as the square root of the distance to threshold of the order parameter, thus highlighting the presence of a supercritical pitchfork bifurcation.

The shape and the thickness of these fingers strongly depend on the stiffness and the thickness of the two layers. As shown in Figure 8(b), the fingers become thicker as we increase α_μ .

We remark that the maximum diameter h of the mesh elements is chosen as the maximum value such that the resulting Δh and $\Delta l/\lambda$ differ by less than 10^{-3} from the corresponding values obtained using a refined mesh with $h/2$.

4.2.2 Case (b): interfacial instability ($\gamma < 0$)

We now focus on the elastic analogue of the Rayleigh Taylor instability, occurring in the configuration depicted in Figure 1(b). Here we set $\alpha_\rho = 2$, so the top layer is heavier than the bottom one.

The simulation results are depicted in Figure 9 for two different values of α_H . In particular, we find a behavior similar to the Rayleigh–Taylor instability in fluids: the displacement is concentrated at the interface of the two layers forming a marginally stable undulation.

Let Δh denote here the maximum vertical distance of the points on the interface between the two layers whilst let Δl be the horizontal distance between the points which have initial coordinates $(\lambda/4, H_a)$ and $(3/4\lambda, H_a)$, so that $\Delta l/\lambda = 0.5$ if $\gamma > \gamma_{cr}$. In Figure 10, we show the nonlinear evolution of such

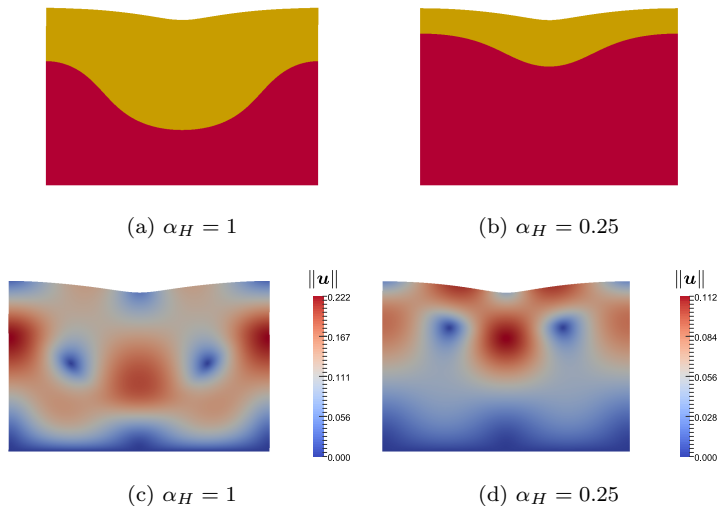


Figure 9: Resulting morphology and displacement fields setting $\alpha_\mu = 1$, $\alpha_\rho = 2$ and (a, c) $\alpha_H = 1$ and $\gamma = -12.36$, (b, d) $\alpha_H = 0.25$ and $\gamma = -21.12$. In (c, d) the colorbars indicate the norm of the displacement.

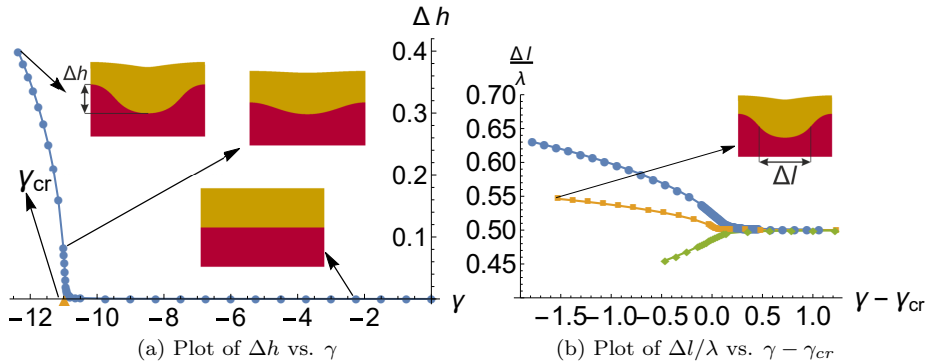


Figure 10: (a) Numerical results showing the height Δh of the undulation versus the order parameter γ , setting $\alpha_\rho = 2$, $\alpha_H = 1$, $\alpha_\mu = 1$. The simulations validate the marginal stability threshold $\gamma_{cr} \simeq -10.97$ predicted by the linear stability analysis. (b) Plot of the normalized undulation thickness $\Delta l/\lambda$ for $\alpha_H = 0.25$ (green), 1 (orange) and 4 (blue).

morphological parameters as a function of γ . As in the previous case, we measured the quantity Δh decreasing the parameter γ finding a continuous increase of the height of the undulation, as reported in Figure 10(a). We highlight that the normalized thickness $\Delta l/\lambda$ strongly depends on the parameter α_H , as we can see from Figure 10(b).

In fact, for thin soft layers the undulation decreases its width whilst decreasing γ beyond its critical value, thus forming a digitation. Conversely, the undulation width increases for thick top layers, thus forming a stable wrinkle. In summary, $\Delta l/\lambda$ increases if the top layer is sufficiently thin, whilst it decreases if the top layer is above a critical thickness. In both cases, the resulting morphology is perfectly reversible after cyclic variations of the order parameters, highlighting the presence of a supercritical pitchfork bifurcation.

5 Discussion and concluding remarks

In this work, we used theoretical and computational tools to investigate the stability of a soft elastic bilayer subjected only to the bulk gravity force.

Assuming that both layers are made of incompressible neo-Hookean materials, we have first formulated the boundary value problem in nonlinear elasticity considering that the slab attached on one end to a rigid substrate and it is traction-free at the other end. Considering the two configurations depicted in Figure 1, we have identified their basic undeformed solutions in Eq. (5), characterized by an hydrostatic pressure linearly varying on the thickness direction.

Secondly, we have studied the linear stability by the means of the method of incremental deformations superposed on the basic elastic solution. We found that both configurations can undergo a morphological transition governed by the order parameter γ , representing the ratio between potential and elastic energies of the top layer. In particular, its critical value depends on three dimensionless parameters: α_H , α_μ , α_ρ representing the thickness, shear moduli and density ratios between the layers, respectively.

Thirdly, we have implemented a finite element code to solve the boundary value problem in the fully nonlinear instability regime. Other than validating the predictions of the linear stability analysis, the simulations have highlighted the nonlinear evolution of the characteristic patterns.

Compared to the classic Rayleigh-Taylor hydrodynamic instability, not surprisingly we have found that elastic effects tend to stabilize the dynamics of the surface undulations forming beyond the linear stability threshold. Nonetheless, we obtained a rich morphological diagram with respect to both geometric and elastic parameters. In the following, we briefly discuss the main results for the two cases under consideration.

If the body hangs below a rigid wall, as depicted in Figure 1(a), we find that there always exists a critical value for the order parameter, driving a morphological transition localised at the free surface. Such a shape instability is favoured if the bottom layer is softer and thicker than the top one, having a critical horizontal wavelength of the same order as the body thickness. In the nonlinear regime, this critical undulation evolves towards forming a digitation, whose characteristic penetration length continuously increases beyond the linear stability threshold, highlighting the existence of a supercritical pitchfork bifurcation.

If the body is attached to a rigid substrate at the bottom surface, as depicted in Figure 1(b), a morphological transition can occur if and only if the top layer has a higher density than the bottom one. Similarly to the previous case, the onset of an elastic bifurcation is favoured by a softer and thicker bottom layer compared to the top one, with a critical wavelength of the same order as the body thickness. However, an important difference is that the shape instability is localised at the interface between the two layers, displaying two characteristic nonlinear patterns. If the top layer is thinner than the bottom one, the undulation evolves towards forming finger-like protrusions, whilst in the opposite geometrical limit a stable wrinkling occurs.

In summary, we have characterized the shape instabilities occurring in a soft elastic bilayer subjected only to the action of the gravity bulk force. Unlike the Rayleigh-Taylor instabilities in fluids, we have demonstrated that the nonlinear elastic effects saturate the dynamic instability of the bifurcated solutions, displaying a rich morphological diagram where both digitations and stable wrinkling can emerge. The results of this work provide important guidelines for the design of novel soft systems with tunable shapes. In fact, the possibility to control by external stimuli both the geometric and the elastic properties in smart materials, such as hydrogels or dielectric elastomers [26], can be used to provoke morphological transitions on demand [27]. Morphological changes in such soft devices may be used, for example, to selectively change the surface roughness (e.g. to perform drag reduction in fluid-structure interactions [28]) or to fabricate tailor-made patterns (e.g. to design adaptive material scaffolds [29]).

A Appendix – Structure of the matrix M

We report the matrix M we used in the equation Eq. (19). We split it into 16 blocks:

$$M = \begin{bmatrix} \mathbf{0} & \mathbf{0} & M_{13} & M_{14} \\ M_{21} & M_{22} & \mathbf{0} & \mathbf{0} \\ M_{31} & M_{32} & M_{33} & M_{34} \\ M_{41} & M_{42} & M_{43} & M_{44} \end{bmatrix},$$

where $\mathbf{0}$ is the null 2×2 matrix and:

$$\begin{aligned} M_{13} &= \begin{bmatrix} \tilde{k} & \alpha_H \tilde{k} + \tilde{k} - 1 \\ -2\tilde{k}\alpha_\mu - \alpha_\rho \gamma & -(\alpha_H + 1)(2\tilde{k}\alpha_\mu + \alpha_\rho \gamma) \end{bmatrix}, \\ M_{14} &= \begin{bmatrix} e^{2\alpha_H \tilde{k}} & e^{2\alpha_H \tilde{k}}(\alpha_H \tilde{k} + \tilde{k} + 1) \\ e^{2\alpha_H \tilde{k}}(2\tilde{k}\alpha_\mu - \alpha_\rho \gamma) & e^{2\alpha_H \tilde{k}}(\alpha_H + 1)(2\tilde{k}\alpha_\mu - \alpha_\rho \gamma) \end{bmatrix}, \quad M_{21} = \begin{bmatrix} 1 & 0 \\ -\tilde{k} & 1 \end{bmatrix}, \\ M_{22} &= \begin{bmatrix} 1 & 0 \\ \tilde{k} & 1 \end{bmatrix}, \quad M_{31} = \begin{bmatrix} 1 & 1 \\ -\tilde{k} & 1 - \tilde{k} \end{bmatrix}, \quad M_{32} = \begin{bmatrix} e^{2\tilde{k}} & e^{2\tilde{k}} \\ e^{2\tilde{k}}\tilde{k} & e^{2\tilde{k}}(\tilde{k} + 1) \end{bmatrix}, \\ M_{33} &= \begin{bmatrix} -1 & -1 \\ \tilde{k} & \tilde{k} - 1 \end{bmatrix}, \quad M_{34} = \begin{bmatrix} -1 & -1 \\ -\tilde{k} & -\tilde{k} - 1 \end{bmatrix}, \\ M_{41} &= \begin{bmatrix} -\tilde{k}(\alpha_H \alpha_\rho \gamma - 2) & \tilde{k}(2 - \alpha_H \alpha_\rho \gamma) - 2 \\ \tilde{k}(\alpha_H \alpha_\rho \gamma - 2) - \gamma & \tilde{k}(\alpha_H \alpha_\rho \gamma - 2) - (\alpha_H \alpha_\rho + 1)\gamma \end{bmatrix}, \\ M_{42} &= \begin{bmatrix} -e^{2\tilde{k}}\tilde{k}(\alpha_H \alpha_\rho \gamma - 2) & e^{2\tilde{k}}(\tilde{k}(2 - \alpha_H \alpha_\rho \gamma) + 2) \\ -e^{2\tilde{k}}(\gamma + \tilde{k}(\alpha_H \alpha_\rho \gamma - 2)) & -e^{2\tilde{k}}(\alpha_H \alpha_\rho \gamma + \gamma + \tilde{k}(\alpha_H \alpha_\rho \gamma - 2)) \end{bmatrix}, \\ M_{43} &= \begin{bmatrix} \tilde{k}(\alpha_H \alpha_\rho \gamma - 2\alpha_\mu) & \alpha_H \tilde{k}\alpha_\rho \gamma - 2(\tilde{k} - 1)\alpha_\mu \\ 2\tilde{k}\alpha_\mu - \alpha_H \tilde{k}\alpha_\rho \gamma + \alpha_\rho \gamma & (\alpha_H + 1)\alpha_\rho \gamma + \tilde{k}(2\alpha_\mu - \alpha_H \alpha_\rho \gamma) \end{bmatrix}, \\ M_{44} &= \begin{bmatrix} \tilde{k}(\alpha_H \alpha_\rho \gamma - 2\alpha_\mu) & \alpha_H \tilde{k}\alpha_\rho \gamma - 2(\tilde{k} + 1)\alpha_\mu \\ -2\tilde{k}\alpha_\mu + \alpha_H \tilde{k}\alpha_\rho \gamma + \alpha_\rho \gamma & (\tilde{k}\alpha_H + \alpha_H + 1)\alpha_\rho \gamma - 2\tilde{k}\alpha_\mu \end{bmatrix}. \end{aligned}$$

B Appendix – Expressions of the coefficients c_j

The coefficient c_1 of equation Eq. (20) is given by

$$\begin{aligned} c_1 &= 2\tilde{k}^2\alpha_\mu(-2(\alpha_\mu^2 - 1)(2\alpha_H^2\tilde{k}^2 + 1)\cosh(2\tilde{k}) + 2(4\alpha_H^2\tilde{k}^4(\alpha_\mu - 1)^2 + \\ &\quad + 2\tilde{k}^2(\alpha_H^2(\alpha_\mu^2 + 1) + 4\alpha_H\alpha_\mu + \alpha_\mu^2 + 1) - (2\tilde{k}^2 + 1)(\alpha_\mu^2 - 1)\cosh(2\alpha_H\tilde{k}) + \alpha_\mu^2 + 1) + \\ &\quad + (\alpha_\mu - 1)^2\cosh(2(\alpha_H - 1)\tilde{k}) + (\alpha_\mu + 1)^2\cosh(2(\alpha_H + 1)\tilde{k})), \end{aligned}$$

whereas c_2 is

$$\begin{aligned} c_2 &= \tilde{k}(4\alpha_H^2\tilde{k}^2\alpha_\rho\alpha_\mu\sinh(2\tilde{k}) - 4\alpha_H^2\tilde{k}^2\alpha_\mu\sinh(2\tilde{k}) + 4\tilde{k}(\alpha_\mu(2\alpha_H\tilde{k}^2(\alpha_H - (\alpha_H + 2)\alpha_\rho) + \alpha_\rho + 1) + \\ &\quad + \alpha_H(2\tilde{k}^2 + 1)\alpha_\rho + \alpha_\mu^2(2\alpha_H\tilde{k}^2 + \alpha_H)) - 4\tilde{k}^2\alpha_\rho\sinh(2\alpha_H\tilde{k}) + 4\tilde{k}^2\alpha_\mu^2\sinh(2\alpha_H\tilde{k}) + \\ &\quad + 4\alpha_H\tilde{k}\cosh(2\tilde{k})(\alpha_\rho - \alpha_\mu^2) - 2\alpha_\mu\cosh(2\alpha_H\tilde{k})(2\tilde{k}(\alpha_\rho - 1) + (\alpha_\rho + 1)\sinh(2\tilde{k})) - 2\alpha_\rho\sinh(2\alpha_H\tilde{k}) + \\ &\quad - \alpha_\rho\sinh(2(\alpha_H + 1)\tilde{k}) + \alpha_\rho\sinh(2\tilde{k} - 2\alpha_H\tilde{k}) - 4\alpha_\mu^2\sinh^2(\tilde{k})\sinh(2\alpha_H\tilde{k}) + \\ &\quad + 4\alpha_\rho\alpha_\mu\sinh(\tilde{k})\cosh(\tilde{k}) - 4\alpha_\mu\sinh(\tilde{k})\cosh(\tilde{k})), \end{aligned}$$

and the expression of c_3 is

$$\begin{aligned} c_3 &= -\frac{1}{2}(\alpha_\rho - 1)\alpha_\rho(2(2\tilde{k}^2(2\alpha_H + \alpha_\mu) - (2\tilde{k}^2 + 1)\alpha_\mu\cosh(2\alpha_H\tilde{k}) - 2\tilde{k}(\alpha_H\sinh(2\tilde{k}) + \\ &\quad + \sinh(2\alpha_H\tilde{k})) + \alpha_\mu) + (\alpha_\mu - 1)\cosh(2(\alpha_H - 1)\tilde{k}) + (\alpha_\mu + 1)\cosh(2(\alpha_H + 1)\tilde{k}) - 2\alpha_\mu\cosh(2\tilde{k})). \end{aligned}$$

Funding

This work has been partially supported by *Progetto Giovani GNFM 2016* funded by the National Group of Mathematical Physics (GNFM - INdAM) and by the MFAG AIRC Grant 17412.

References

- [1] T. Tanaka, S.-T. Sun, Y. Hirokawa, S. Katayama, J. Kucera, Y. Hirose, and T. Amiya, “Mechanical instability of gels at the phase transition,” *Nature*, vol. 325, no. 6107, pp. 796–798, 1987.
- [2] J. Dervaux and M. B. Amar, “Mechanical instabilities of gels,” *Annu. Rev. Condens. Matter Phys.*, vol. 3, no. 1, pp. 311–332, 2012.
- [3] J. Kim, J. A. Hanna, M. Byun, C. D. Santangelo, and R. C. Hayward, “Designing responsive buckled surfaces by halftone gel lithography,” *Science*, vol. 335, no. 6073, pp. 1201–1205, 2012.
- [4] J. Zhu, H. Stoyanov, G. Kofod, and Z. Suo, “Large deformation and electromechanical instability of a dielectric elastomer tube actuator,” *Journal of Applied Physics*, vol. 108, no. 7, p. 074113, 2010.
- [5] C. Keplinger, T. Li, R. Baumgartner, Z. Suo, and S. Bauer, “Harnessing snap-through instability in soft dielectrics to achieve giant voltage-triggered deformation,” *Soft Matter*, vol. 8, no. 2, pp. 285–288, 2012.
- [6] L. Rayleigh, “On the capillary phenomena of jets,” *Proc. R. Soc. London*, vol. 29, no. 196-199, pp. 71–97, 1879.
- [7] S. Mora, T. Phou, J.-M. Fromental, L. M. Pismen, and Y. Pomeau, “Capillarity driven instability of a soft solid,” *Physical Review Letters*, vol. 105, no. 21, p. 214301, 2010.
- [8] M. Taffetani and P. Ciarletta, “Beading instability in soft cylindrical gels with capillary energy: Weakly non-linear analysis and numerical simulations,” *Journal of the Mechanics and Physics of Solids*, vol. 81, pp. 91–120, 2015.
- [9] P. G. Saffman and G. Taylor, “The penetration of a fluid into a porous medium or Hele-Shaw cell containing a more viscous liquid,” *Proceedings of the Royal Society of London A: Mathematical, Physical and Engineering Sciences*, vol. 245, no. 1242, pp. 312–329, 1958.
- [10] B. Saintyves, O. Dauchot, and E. Bouchaud, “Bulk elastic fingering instability in hele-shaw cells,” *Physical Review Letters*, vol. 111, no. 4, p. 047801, 2013.
- [11] A. Ghatak, M. K. Chaudhury, V. Shenoy, and A. Sharma, “Meniscus instability in a thin elastic film,” *Physical Review Letters*, vol. 85, no. 20, p. 4329, 2000.

- [12] S. Mora, T. Phou, J.-M. Fromental, and Y. Pomeau, “Gravity Driven Instability in Elastic Solid Layers,” *Physical Review Letters*, vol. 113, no. 17, p. 178301, 2014.
- [13] X. Liang and S. Cai, “Gravity induced crease-to-wrinkle transition in soft materials,” *Applied Physics Letters*, vol. 106, no. 4, p. 041907, 2015.
- [14] F. Auricchio, L. B. Da Veiga, C. Lovadina, A. Reali, R. L. Taylor, and P. Wriggers, “Approximation of incompressible large deformation elastic problems: some unresolved issues,” *Computational Mechanics*, vol. 52, no. 5, pp. 1153–1167, 2013.
- [15] F. Auricchio, L. B. da Veiga, C. Lovadina, and A. Reali, “A stability study of some mixed finite elements for large deformation elasticity problems,” *Computer Methods in Applied Mechanics and Engineering*, vol. 194, no. 9, pp. 1075–1092, 2005.
- [16] F. Auricchio, L. B. Da Veiga, C. Lovadina, and A. Reali, “The importance of the exact satisfaction of the incompressibility constraint in nonlinear elasticity: mixed FEMs versus NURBS-based approximations,” *Computer Methods in Applied Mechanics and Engineering*, vol. 199, no. 5, pp. 314–323, 2010.
- [17] L. Rayleigh, “Investigation of the character of the equilibrium of an incompressible heavy fluid of variable density,” *Proc. London Math. Soc.*, vol. 14, no. 1, p. 8, 1883.
- [18] G. Taylor, “The instability of liquid surfaces when accelerated in a direction perpendicular to their planes. I,” *Proceedings of the Royal Society of London A: Mathematical, Physical and Engineering Sciences*, vol. 201, no. 1065, pp. 192–196, 1950.
- [19] M. Fermigier, L. Limat, J. Wesfreid, P. Boudinet, and C. Quilliet, “Two-dimensional patterns in Rayleigh-Taylor instability of a thin layer,” *Journal of Fluid Mechanics*, vol. 236, pp. 349–383, 1992.
- [20] R. W. Ogden, *Non-linear elastic deformations*. Courier Corporation, 1997.
- [21] A. Logg, K.-A. Mardal, and G. Wells, *Automated solution of differential equations by the finite element method: The FEniCS book*, vol. 84. Springer Science & Business Media, 2012.
- [22] D. Boffi, F. Brezzi, M. Fortin, *et al.*, *Mixed finite element methods and applications*, vol. 44. Springer, 2013.
- [23] P. Ciarletta, V. Balbi, and E. Kuhl, “Pattern selection in growing tubular tissues,” *Physical Review Letters*, vol. 113, no. 24, p. 248101, 2014.
- [24] P. Ciarletta, M. Destrade, A. Gower, and M. Taffetani, “Morphology of residually stressed tubular tissues: Beyond the elastic multiplicative decomposition,” *Journal of the Mechanics and Physics of Solids*, vol. 90, pp. 242–253, 2016.

- [25] S. Budday, E. Kuhl, and J. W. Hutchinson, “Period-doubling and period-tripling in growing bilayered systems,” *Philosophical Magazine*, vol. 95, no. 28-30, pp. 3208–3224, 2015.
- [26] R. Pelrine, R. D. Kornbluh, J. Eckerle, P. Jeuck, S. Oh, Q. Pei, and S. Stanford, “Dielectric elastomers: generator mode fundamentals and applications,” in *SPIE’s 8th Annual International Symposium on Smart Structures and Materials*, pp. 148–156, International Society for Optics and Photonics, 2001.
- [27] A. Sydney Gladman, E. A. Matsumoto, R. G. Nuzzo, L. Mahadevan, and J. A. Lewis, “Biomimetic 4D printing,” *Nat Mater*, vol. 15, pp. 413–418, Apr 2016.
- [28] B. Dean and B. Bhushan, “Shark-skin surfaces for fluid-drag reduction in turbulent flow: a review,” *Philosophical Transactions of the Royal Society of London A: Mathematical, Physical and Engineering Sciences*, vol. 368, no. 1929, pp. 4775–4806, 2010.
- [29] K. Saha, J. Kim, E. Irwin, J. Yoon, F. Momin, V. Trujillo, D. V. Schaffer, K. E. Healy, and R. C. Hayward, “Surface creasing instability of soft polyacrylamide cell culture substrates,” *Biophysical journal*, vol. 99, no. 12, pp. L94–L96, 2010.

MOX Technical Reports, last issues

Dipartimento di Matematica
Politecnico di Milano, Via Bonardi 9 - 20133 Milano (Italy)

- 58/2016** Antonietti, P. F.; Bruggi, M. ; Scacchi, S.; Verani, M.
On the Virtual Element Method for Topology Optimization on polygonal meshes: a numerical study
- 56/2016** Guerciotti, B.; Vergara, C.; Ippolito, S.; Quarteroni, A.; Antona, C.; Scrofani, R.
A computational fluid-structure interaction analysis of coronary Y-grafts
- 57/2016** Bassi, C.; Abbà, A.; Bonaventura, L.; Valdetaro, L.
Large Eddy Simulation of gravity currents with a high order DG method
- 55/2016** Antonietti, P. F.; Facciola' C.; Russo A.; Verani M.;
Discontinuous Galerkin approximation of flows in fractured porous media on polytopic grids
- 54/2016** Vergara, C.; Le Van, D.; Quadrio, M.; Formaggia, L.; Domanin, M.
Large Eddy Simulations of blood dynamics in abdominal aortic aneurysms
- 53/2016** Antonietti, P. F.; Manzini, G.; Verani, M.
The fully nonconforming Virtual Element method for biharmonic problems
- 52/2016** Paolucci, R.; Evangelista, L.; Mazzieri, I.; Schiappapietra, E.
The 3D Numerical Simulation of Near-Source Ground Motion during the Marsica Earthquake, Central Italy, 100 years later
- 51/2016** Guzzetti, S.; Perotto, S.; Veneziani, A.
Hierarchical Model Reduction for Incompressible Flows in Cylindrical Domains: The Axisymmetric Case
- 50/2016** Ambrosi, D.; Pezzuto, S.; Riccobelli, D.; Stylianopoulos, T.; Ciarletta, P.
Solid tumors are poroelastic solids with a chemo--mechanical feedback on growth
- 49/2016** Formaggia, L.; Scotti, A.; Sottocasa, F.
ANALYSIS OF A MIMETIC FINITE DIFFERENCE APPROXIMATION OF FLOWS IN FRACTURED POROUS MEDIA